Met. Mater. Int., Vol. 22, No. 5 (2016), pp. 810~816
doi: 10.1007/s12540-016-6113-7

Characterization of Twin-Like Structure in a Ferrite-Based Lightweight Steel

Pooriya Dastranjy Nezhadfar[1], Abbas Zarei-Hanzaki[1,*], Seok Su Sohn[2], and Hamid Reza Abedi[1]

[1]School of Metallurgy and Materials Engineering, College of Engineering, University of Tehran,
The complex Laboratory of Hot Deformation & Thermo-mechanical Processing of High
Performance Engineering Materials, Tehran 111554563, Iran
[2]Center for Advanced Aerospace Materials, Pohang University of Science and Technology,
Pohang 37673, Republic of Korea

(received date: 12 February 2016 / accepted date: 27 March 2016)

The present study examined cold to warm compressive deformation behavior of a ferrite- based lightweight steel through characterization of the banded structures. Compression tests were carried out at 25 to 500 °C at a strain rate of 0.01 s^{-1} up to true strain of 0.6. Analysis of the microstructural evolution using electron back scatter diffraction indicated that the twin-like bands in the large ferrite grains occurred with the {112}[111] system at a 60° misorientation. Density of the twin-like bands is increased by raising the deformation temperature. EBSD results showed that the primary and secondary twins occurred in the [-11-1] and [1-1-1] directions. In addition, the strain at 500 °C distorted the twin-like bands and resulted in wavy boundaries. The strain hardening behavior was also examined using the Crussard-Jaoul (C-J) model and the n-values were calculated for each stage of imposing strain. The results showed high dislocation density in the adjacent of twin-like boundaries intersections which resulted in the n-value increment.

Keywords: metals, ferrite-based lightweight steel, thermo-mechanical processing, twinning, electron backscattering diffraction (EBSD), mechanical properties

1. INTRODUCTION

Global warming and environmental pollution have produced catastrophic effects globally. Car manufacturing companies have responded to this by focusing on ways to reduce the weight of vehicles to improve fuel efficiency and decrease exhaust emissions [1,2]. The most efficient method to accomplish this, is the use of lightweight materials. Many efforts have been directed towards development of the lightweight materials such as Al [3,4] and Mg alloys [5,6], despite their high cost. These alloys are not be appropriate for all parts and components, especially the frame, because they possess insufficient mechanical and joining properties. To address this deficiency, several types of high-strength steels, such as dual-phase [7,8], transformation-induced plasticity (TRIP) steels [9-11] and twinning induced plasticity (TWIP) steels [1,12,13] have been introduced.

Although, such steels show high strength and formability, a decrease in weight has yet to be achieved. Studies have sought to develop steel having a lower density [14]. Lightweight steel has been developed by substituting heavy elements with lighter ones, such as aluminum and silicon [15,16]. The addition of 5-6% Al would result in 8 to 10% weight savings in comparison with conventional Fe-Mn-Al-C steels [14,17]. These steels have been categorized into ferrite based [18-20] and austenite based duplex ($\alpha + \gamma$) [21,22] or Triplex ($\alpha + \gamma + \kappa$-carbides) steels [23,24]. Among these lightweight steels, the austenitic or (austenite + ferrite) duplex ones are considered for ultra-high-strength applications since the austenite could exhibit various strengthening mechanisms. Park *et al.* [25] reported that the deformation induced martensite transformation in low density steel with 5% Al content produced excellent mechanical properties (high tensile strength of >900 MPa with total elongation of >50%). In another study authors [26] reported 77% ductility as well as high tensile strength (734 MPa) in a duplex lightweight steel. These enhanced properties were attributed to the simultaneous formation of deformation induced martensite and deformation twins in austenite. Furthermore it is believed that the high aluminum content as ferrite stabilizer shall be compensated by Mn content to stabilize the austenite [27]. On the other hand, high aluminum content would increase the stacking fault energy of austenite [28,29]. Park *et al.* [22] have reported that, regardless of high stacking fault energy in austenite, the substructures associated with planar glide such as Taylor lattice, Taylor lattice domain boundaries and microbands were progressively developed during straining. In addition to the well-known banded structures like TWin-

---

*Corresponding author: zareih@ut.ac.ir

ning Induced Plasticity (TWIP) and TRansformation Induced Plasticity (TRIP), the occurrence of MicroBand Induced Plasticity (MBIP) has been also reported in austenitic low density steels [30]. Although many studies have reported on the characterization of banded structures in austenitic steels, ferrite-based lightweight steels have not received much attention. Accordingly, the present study investigated the possibility and character of banded structures in ferrite-based lightweight steel. To this end, the compression tests were performed and the advanced characterization methods were employed to examine the microstructural evolution.

2. EXPERIMENTAL PROCEDURES

The experimental lightweight steel with the composition of Fe-0.07C-11.15Mn-5.6Al-0.12Si (wt%) received in an electroslag remelted state. Figure 1 is a schematic representation of the processing steps applied to the alloy. The remelted material was homogenized at 1200 °C for 1 hour and then subjected to 5 passes of hot rolling at temperatures in the range of 1200-900 °C followed by air quenching. The apparent density was measured 7.1 g.cm^{-3} using a proper densitometer (Mettler-Toledo XP205, Mettler-Toledo AG) based on Archimedes principle, which shows considerable reduction in comparison with pure Fe [27]. The specimen was weighed in a high precision balance and the volume of water displaced by it, while immersed in a volumetric tube, was measured. The accuracy of the measurement in the two cases were 0.01 g and 1 ml, respectively. For each measurement a specimen volume of ~5000 mm^3 was used. The hot rolled material was annealed at 1200 °C for 25 minutes followed by water quenching to achieve a dual phase structure with the highest ferrite fraction in the microstructure.

In order to conduct compression testing, the cylindrical specimens with 8 mm diameter and 12 mm height according to ASTM-E209 standard [31] were machined from the annealed material. Compression tests were performed at 25 to 500 °C under a strain rate of 0.01 s^{-1} using GOTHECH AL-7000 LA 30 testing machine. Thermomechanical processing ended when water was used to quench the deformed specimens. In order to confirm the repetitiveness of the results each test repeated 3 times. In addition, some interruptions were conducted to investigate the microstructural evolution precisely.

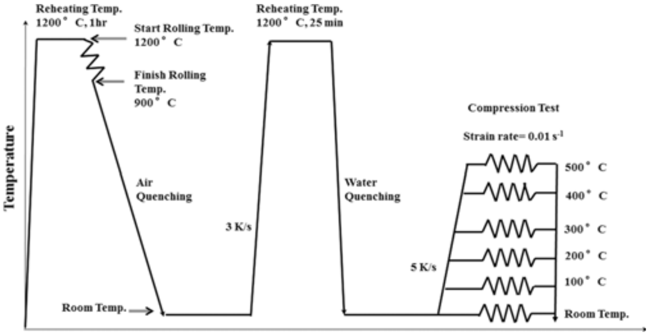

Fig. 1. The schematic presentation of processing cycles.

Optical microscopy and scanning electron microscopy (SEM) were used to examine the obtained microstructure. To follow these, the specimens were sectioned in parallel to the compression axis and then treated through conventional metallographical surface preparation methods. Specimens were then etched by 2% Nital solution followed by Marshal solution (Part A: 5 ml Sulfuric acid, 8 gr Oxalic acid, 100 ml water-Part B: 30% solution hydrogen peroxide). X-ray diffraction analysis was carried out using Philips-X'pert instrument to identify the constitutive phases. In these tests, the polished samples were exposed to Cu-Kα radiation (Kα = 1.54056 Å) in the 2θ range of 20-100° with an accelerating voltage of 40 kV and a scanning speed of 2° min^{-1}. The volume fraction of phases were measured by direct comparison method [32]. Integrated intensities of $(200)_\alpha$ and $(211)_\alpha$ peaks and $(220)_\gamma$ and $(113)_\gamma$ were used for this XRD method. Furthermore, the optical image analyzing method with Clemex Software was used to measure the grain size. Electron back scatter diffraction (EBSD) was performed using a field emission scanning electron microscope (FE-SEM; Quanta 3D FEG, FEI Company, USA). The EBSD specimens were electro-polished at room temperature in a solution of CH_3COOH (92%) and $HClO_4$ (8%) at an operating voltage of 32 V. The data were then interpreted by orientation imaging microscopy (OIM) analysis software provided by Tex SEM Laboratories, Inc.

3. RESULTS AND DISCUSSION

The XRD pattern and the optical microstructure of the annealed specimen at 1200 °C for 25 minutes are shown in Figs. 2a and b. The XRD pattern in Fig. 2a, indicates that the majority of phase fraction is ferrite. In addition, in the optical microstructure the matrix is ferrite, and the austenite grains

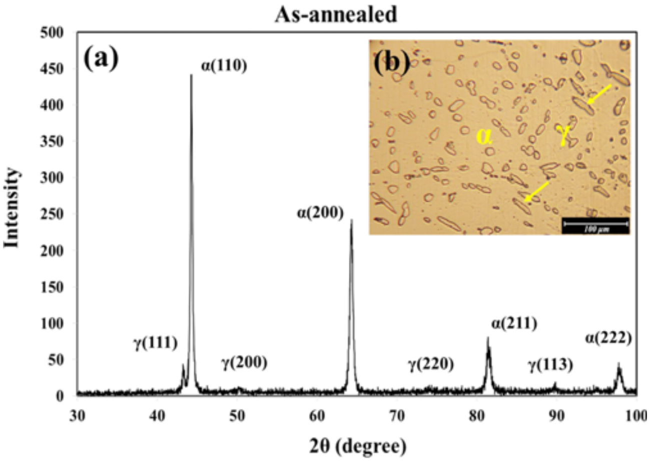

Fig. 2. (a) As annealed specimen's XRD pattern, and (b) the optical microstructure of annealed specimen at 1200 °C for 25 min.

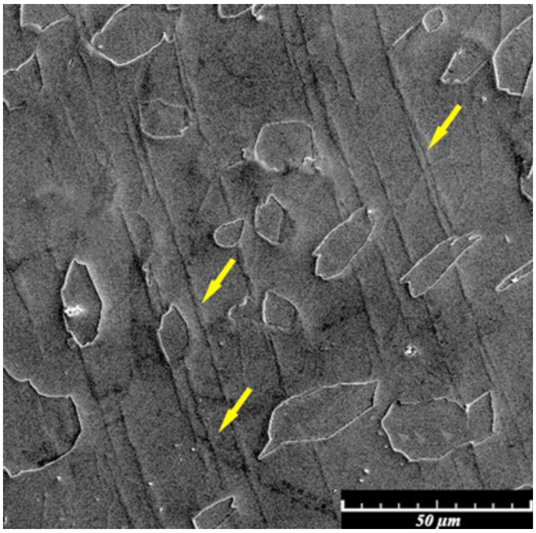

Fig. 3. SEM micrograph of compressed specimen up to the true strain of 0.6 at room temperature (arrows show the deformation bands).

are uniformly distributed in the matrix. The austenite grain size was approximately 15 μm, but the ferrite grains were coarse and approximately 500 μm. The volume fractions measured by XRD and image analyzer are in compatible, and the ferrite and austenite fractions at room temperature were approximately 86% and 14%, respectively.

Figure 3 shows SEM micrograph of compressed specimen at room temperature. As seen, parallel deformation bands formed in the coarse ferrite grains. The interspace of these bands is between 10 to 30 μm and the thickness of the deformation bands is approximately 1 μm.

EBSD was performed to understand the nature of the deformation bands. The inverse pole figure, phase map, image quality and boundary map of interrupted compression test at room temperature (deformed up to 0.15 true strain) are shown in Fig. 4. It is shown that, these deformation bands are presented even at the early stages of deformation. The image quality (IQ) map combined with the boundary map in Fig. 4c depicts that these deformation bands hold high angle rotation. The misorientation angle of the deformation bands in relation to the matrix is denoted by the black arrow in the <111> direc-

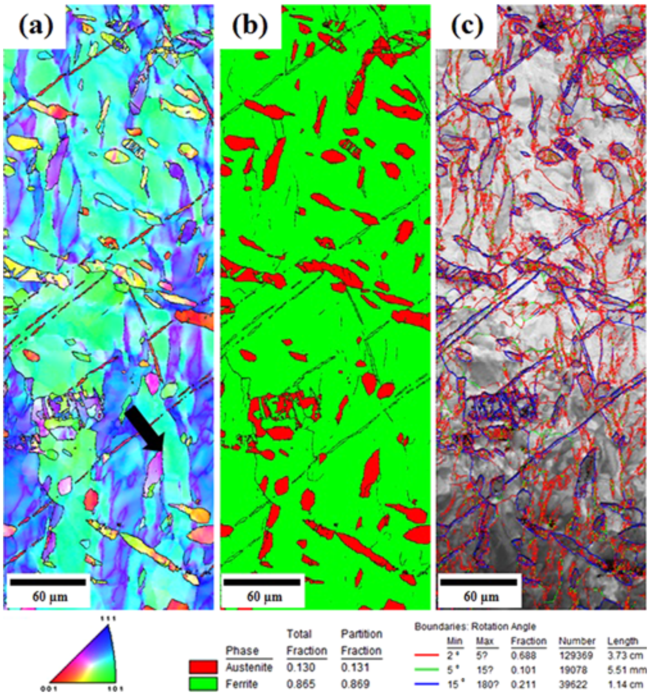

Fig. 4. EBSD results for the specimen deformed up to the true strain of 0.15: (a) inverse pole figure (b) phase map (c) image quality and boundary map of ND planes.

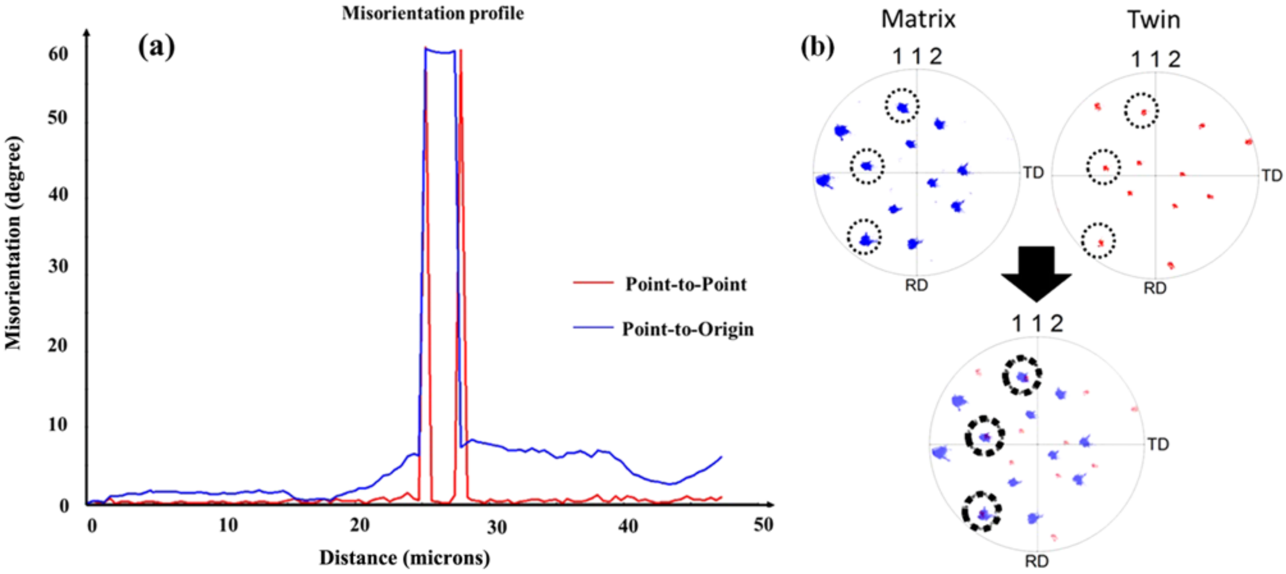

Fig. 5. (a) Misorientation profile of the region indicated by black arrow in Fig. 4a, and (b) {112} pole figure of deformation band and matrix which shows a triple point coincidence.

tion (Fig. 4a), is provided in Fig. 5a. As seen, the misorientation between these bands and the matrix is approximately 60°. In addition the {112} pole figure of deformation bands and the ferritic matrix in Fig. 5b shows the triple point coincident corresponding to the deformation bands and matrix. These results (misorientation angle of ~60° and the triple point coincident on the {112} plane) indicate that these deformation bands are in twin relation with the matrix [33-35].

It is well established that deformation twinning would occur in large grain bcc materials in {112}[111] system as a result of screw dislocation dissociation [36]. It has been well proved that the dislocation dissociation might have been activated in low to intermediate temperatures or under medium to high strain rates [35,37-39]. As Lagerlof [37] pointed out, in these circumstances, due to the <111> dislocation slip limitations, the dislocation would be dissociated into three partial ones on the three {112} planes. It has been proposed by Vitek [40,41] that in bcc, twins are multi-layered stacking faults created by the passage of aforementioned partial dislocations. Figure 6 illustrates the schematic sequential process of shearing consecutive {112} planes of bcc crystal to form a twin. As seen, the partials would rearrange the stacking of these planes to form three-layered stacking fault and steered it to twin stacking [42].

Figure 7 shows the SEM micrographs of compressed specimens at 100 to 500 °C. The features of deformation at 100 °C (Fig. 7a) were similar to those at room temperature (Fig. 3). Surprisingly, the frequency of twin-like bands is increased by increasing the test temperature to higher values. Furthermore, intersections can be observed (denoted by red arrows) in Fig. 7c and the interspace between bands decreased to ~1-4 µm. Figs. 7d and e show the compressed specimens at 400 °C and 500 °C, respectively. It can be seen that the twin-like bands are distorted and characterized by wavy boundaries. Figure 8 depicts the misorientation profiles and {112} plane pole figures of the compressed specimens at 300 °C and 500 °C. In these deformation conditions, the twin-like bands have also 60° misorientation angel to the matrix (Figs. 8a and c). Fig. 8b and d show the triple point coincident of bands' poles (red and blue) with the matrix ones (gray) in {112} plane. In order to investigate the effect of high frequency banding on the strain hardening behavior of the material, the compressed specimen at 300 °C is considered. Figure 9a shows the trues stress- true strain and its corresponding strain hardening curve. As seen, there are four distinct stages, which are designated by stages A, B, C and D. After a dramatic decrease of strain hardening in stage A, the strain hardening rate increases to constant level at stage B. Subsequently, the strain hardening rate is decreased abruptly at stage C and eventually it is increased to constant level at stage D.

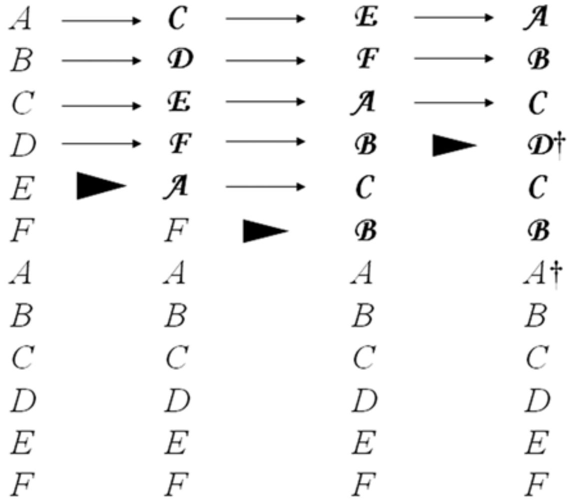

Fig. 6. An illustration of the stacking sequence formed when three 1/6 [111] partials on adjacent {112} planes, moves to the right on a glide plane between F and A. Locally a BCDCBABC... micro-twin is formed where the two twin planes are indicated with †.

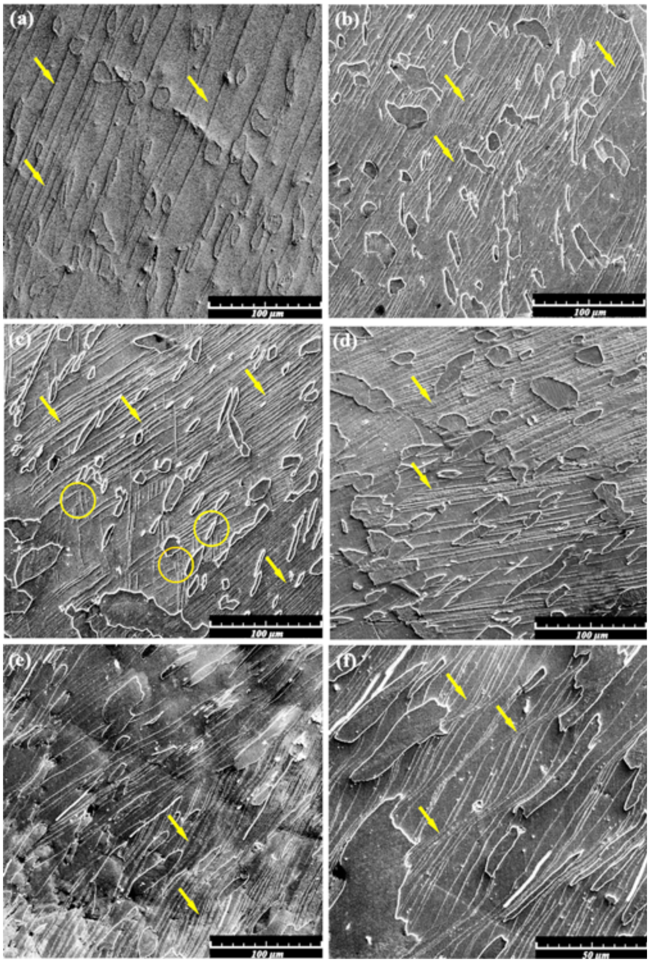

Fig. 7. SEM micrographs of compressed specimens up to the true strain of 0.6 at: (a) 100 °C, (b) 200 °C, (c) 300 °C, (d) 400 °C, and (e) 500 °C. (f) Higher magnification of 500 °C.

The true stress-strain curve examined using several empirical fitting formulae and mathematical analysis to determine

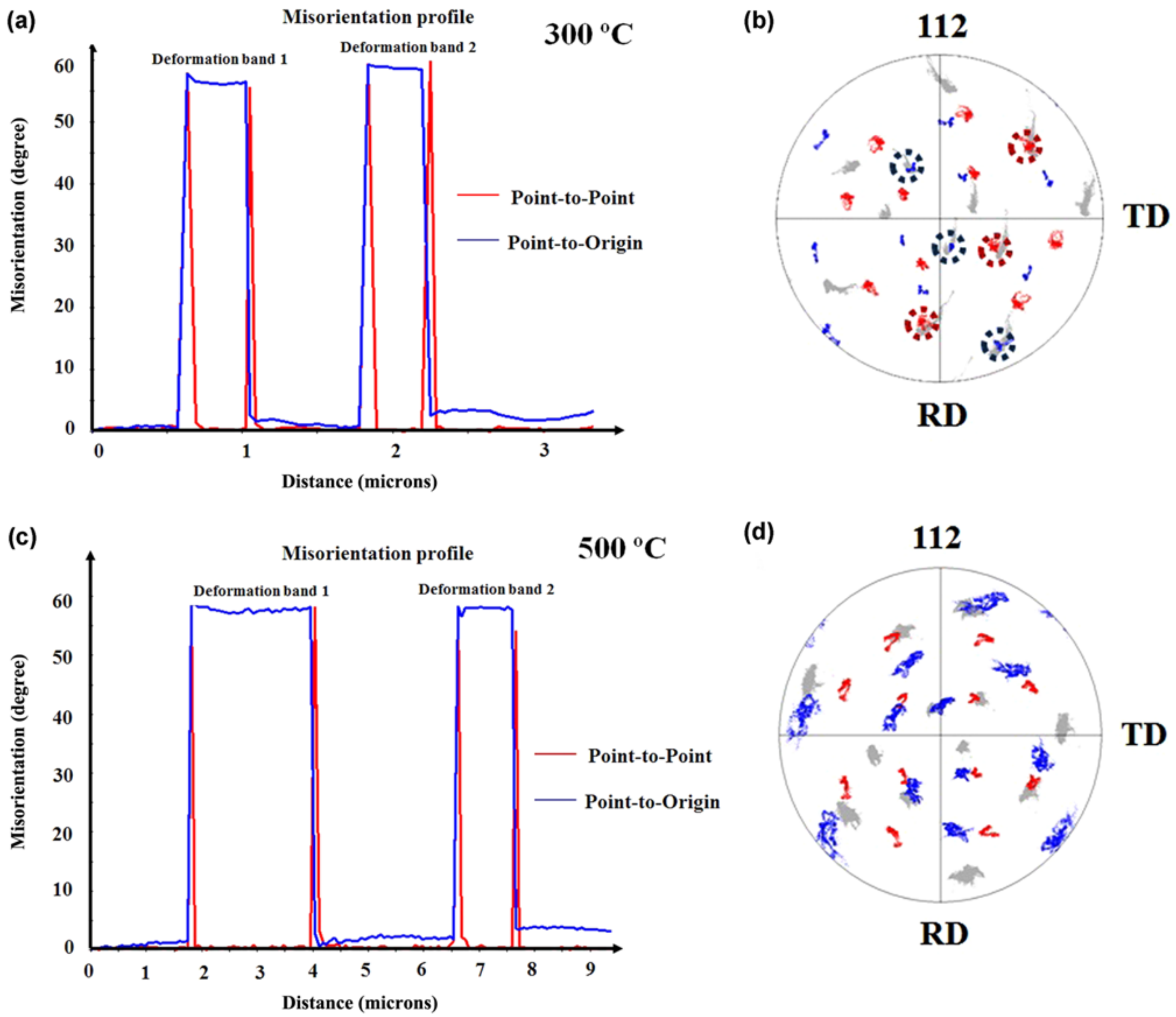

Fig. 8. Misorientation profile and {112} pole figure of deformation bands and matrix for compressed specimens at: (a) and (b) 300 ºC, (c) and (d) 500 °C.

the strain hardening behavior at each stage. Modified C-J analysis most clearly distinguished strain hardening stages in a $\ln(d\sigma/d\varepsilon)$–$\ln\sigma$ plot (Fig. 9b) [43,44]. This plot clearly shows stages A, B, C, and D at different slopes $(1-1/n)$ at the critical strains of ε_B, ε_C, and ε_D. The n values of stages A, B, C, and D, are 0.34, 2.2, 0.15, and 0.3, and the critical strains are 0.14, 0.3, and 0.45, respectively. As is well established the decrease in stage A relates to the onset of dislocation movements [44,45]. As was aforementioned the deformation twin-like bands had been formed at the early stage of deformation (below 0.15 true strain). By imposing strain beyond ε_B to ε_C, the n value at stage B strongly increased from the eruption of twin-like band formation with similar growth directions. This was accompanied by a decrease in band interspaces. It appears that the twin-like bands with high angle boundaries are strong barriers to dislocation movements which is in agreement with [46], thus the stress level would increase. The strain hardening is decreased beyond ε_C to ε_D at stage C; this is attributed to the twin-like bands generation super-saturation. In addition, the twin-like bands appear to reorient the matrix lattice to stimulate the further dislocation slip (in agreement with [35]). By imposing strain to higher values, at stage D, the n value is increased due to the formation of secondary twin-like bands. Accordingly, to trace the occurrence of secondary twin-like bands in stage D, the compression tests were interrupted at 0.25 true strain (within stage B) and 0.55 true strain (within stage D). Figure 10a shows the microstructure of compressed specimen at stage B. As is obvious the primary deformation twins with the interspace of approximately 1-4 μm are elongated in the coarser grains. The direction of primary twin-like bands is found out using EBSD analysis to be [-11-1]. On the other hand, Figure 10b shows that the second-

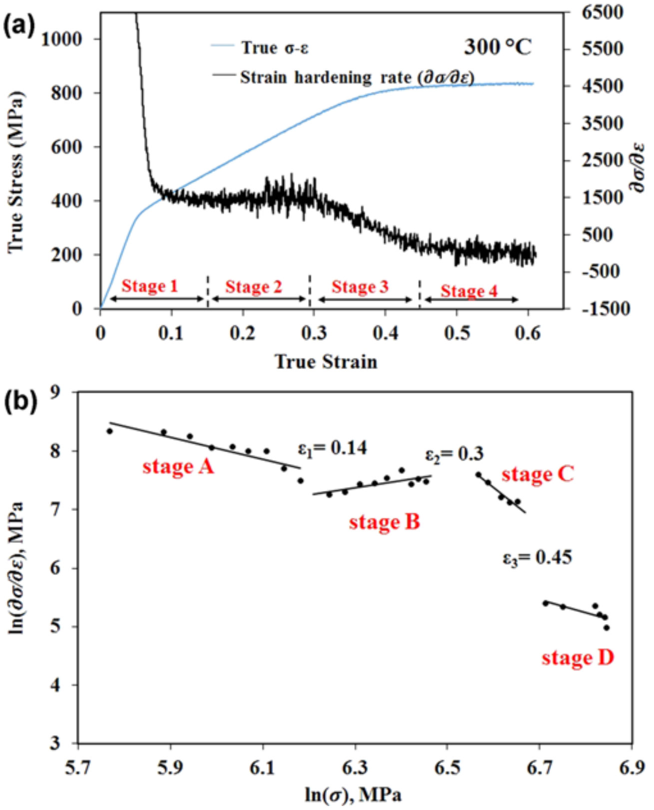

Fig. 9. (a) the strain hardening rate curve of compressed specimen at 300 °C, and (b) the plot of ln(∂σ/∂ε) vs. lnσ based on the modified Crussard-Jaoul analysis of the stress-strain curve used to examine the strain hardening exponents in the plastic deformation region.

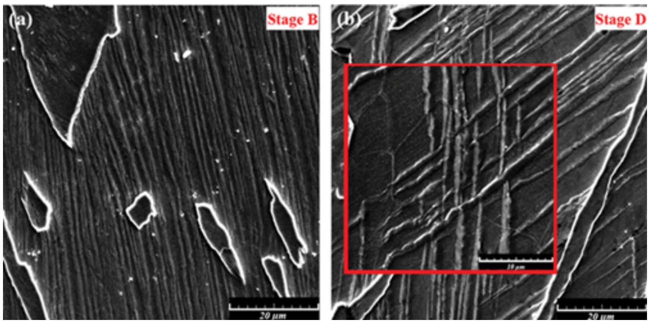

Fig. 10. Interrupted tests at: (a) true strain of 0.25 (stage B), (b) true strain of 0.55 (stage D).

ary twin-like bands, which are formed at stage D, are developed along the [1-1-1] direction. Figure 11a shows the inverse pole figure of compressed specimen at 300 °C for stage D. The deformation band 1 and 2 directions have been presented. As seen the secondary bands are intersected with primary ones and have subdivided the coarse grains to smaller areas. Figure 11b shows the corresponded KAM analysis. It can be seen that the dislocation density is higher at the vicinity of twin-like boundaries than that of other regions which are denoted by black arrows. This justifies the fact that the twin-like boundaries in ferrite matrix may act as strong barriers to dislocation movements and would lead to the higher n values in the final stage (stage D) of deformation.

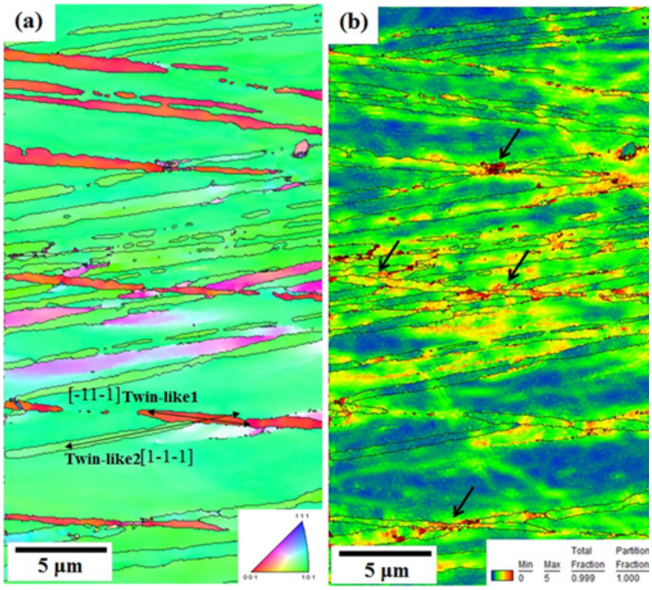

Fig. 11. (a) Inverse pole figure of specimen compressed up to 0.55 true strain (stage D) shows the intersection of twin-like bands, and (b) the corresponding Kernel Average Measurement shows higher dislocation density at the vicinity of twin-like intersections.

4. CONCLUSION

Twin-like banded structures, which were developed during cold to warm deformation of Fe-0.07C-11.15Mn-5.6Al-0.12Si (wt%) ferrite-based lightweight steel, were investigated in the present investigation. The following results were obtained:

(1) The EBSD results revealed that the steel is highly capable for development of banded structures. From the misorientation angle of ~60° and the triple point coincident on the {112} plane, it was concluded that the deformation bands are in twin relation with the matrix.

(2) The frequency of deformation twin-like bands were increased by raising the compression test temperature and intersections of them were observed at 300 °C.

(3) The strain hardening rate showed four distinct stages. The n-values for each stage up to the corresponding critical strain were calculated using the C-J model. This showed that the n-value increased from 0.34 to 2.2 from stage A to B, respectively due to the higher banding frequency. Furthermore, the generation of secondary bands at higher strains, in stage D, increased the n value, either.

REFERENCES

1. H. Aydin, I.-H. Jung, E. Essadiqi, and S. Yue, *Mat. Sci. Eng. A* **591**, 90 (2014).

2. R. Rana, C. Liu, and R. K. Ray, *Acta Mater.* **75**, 227 (2014).
3. N. Haghdadi, A. Zarei-Hanzaki, A. A. Roostaei, and A. Hemmati, *Mater. Design* **43**, 419 (2013).
4. N. Haghdadi, A. Zarei-Hanzaki, H. Abedi, and O. Sabokpa, *Mat. Sci. Eng. A* **549**, 93 (2012).
5. M. Maghsoudi, A. Zarei-Hanzaki, and H. Abedi, *Mat. Sci. Eng. A* **595**, 99 (2014).
6. S. Fatemi-Varzaneh, A. Zarei-Hanzaki, and M. Haghshenas, *J. Alloys. Compd.* **475**, 126 (2009).
7. A. Imandoust, A. Zarei-Hanzaki, S. Heshmati-Manesh, S. Moemeni and P. Changizian, *Mater. Design* **53**, 99 (2014).
8. D. Bombac, M. Peet, S. Zenitani, S. Kimura, T. Kurimura, and H. Bhadeshia, *Mater. Sci. Eng.* **22**, 045005 (2014).
9. C. Herrera, D. Ponge, and D. Raabe, *Acta Mater.* **59**, 4653 (2011).
10. M. M. Wang, C. C. Tasan, D. Ponge, A. Kostka, and D. Raabe, *Acta Mater.* **79**, 268 (2014).
11. A. Mohamadizadeh, A. Zarei-Hanzaki, S. Heshmati-Manesh, and A. Imandoust, *Mat. Sci. Eng. A* **607**, 621 (2014).
12. P. Dastranjy Nezhadfar, A. Rezaeian, and M. S. Sojudi Papkiadeh, *J. Mater. Eng. Perform.* **24**, 3820 (2015).
13. B. Qin and H. K. D. H. Bhadeshia, *Mater. Sci. Technol.* **24**, 969 (2008).
14. D.-W. Suh and N. J. Kim, *Scripta Mater.* **68**, 337 (2013).
15. M. C. Ha, J.-M. Koo, J.-K. Lee, S. W. Hwang, and K.-T. Park, *Mat. Sci. Eng. A* **586**, 276 (2013).
16. Y.-U. Heo, Y.-Y. Song, S.-J. Park, H. K. D. H. Bhadeshia, and D.-W. Suh, *Metall. Mater. Trans. A* **43**, 1731 (2012).
17. H. Kim, D.-W. Suh, and N. J. Kim, *Sci. Tech. Adv. Mater.* **14**, 014205 (2013).
18. S. S. Sohn, B. J. Lee, S. Lee, and J. H. Kwak, *Acta Mater.* **61**, 5626 (2013).
19. J. B. Seol, D. Raabe, P. Choi, H. S. Park, J. H. Kwak, and C. G. Park, *Scripta Mater.* **68** 348 (2013).
20. A. Zargaran, H. S. Kim, J. H. Kwak, and N. J. Kim, *Scripta Mater.* **89**, 37 (2014).
21. D. Raabe, H. Springer, I. Gutierrez-Urrutia, F. Roters, M. Bausch, J.-B. Seol, M. Koyama, P.-P. Choi, and K. Tsuzaki, *JOM* **66**, 1845 (2014).
22. K.-T. Park, *Scripta Mater.* **68**, 375 (2013).
23. A. Etienne, V. Massardier-Jourdan, S. Cazottes, X. Garat, M. Soler, I. Zuazo, and X. Kleber, *Metall. Mater. Trans. A* **45**, 324 (2014).
24. G. Frommeyer and U. Brüx, *Steel Research International* **77**, 627 (2006).
25. S. J. Park, B. Hwang, K. H. Lee, T. H. Lee, D. W. Suh, and H. N. Han, *Scripta Mater.* **68**, 365 (2013).
26. S. S. Sohn, K. Choi, J.-H. Kwak, N. J. Kim, and S. Lee, *Acta Mater.* **78**, 181 (2014).
27. S. S. Sohn, H. Song, B.-C. Suh, J.-H. Kwak, B.-J. Lee, N. J. Kim, and S. Lee, *Acta Mater.* **96**, 301 (2015).
28. W. S. Yang and C. M. Wan, *J. Mater. Sci.* **25**, 1821 (1990).
29. D. Pierce, J. Jiménez, J. Bentley, D. Raabe, and J. Wittig, *Acta Mater.* **100**, 178 (2015).
30. J. D. Yoo and K.-T. Park, *Mat. Sci. Eng. A* **496**, 417 (2008).
31. *Standard Practice for Compression Tests of Metallic Materials at Elevated Temperatures with Conventional or Rapid Heating Rates and Strain Rates,* vol.03.01, ASTM International, ASTM E209 (2010).
32. D.-W. Suh, S.-J. Park, T.-H. Lee, C.-S. Oh and S.-J. Kim, *Metall. Mater. Trans. A* **41**, 397 (2009).
33. D. F. W. S. Mahajan, *International Metallurgical Reviews* **18**, 43 (1973).
34. G. S. R. Hossein Beladi, *Acta Mater.* **61**, 9 (2013).
35. J. Xie, H. Fu, Z. Zhang, and Y. Jiang, *Mat. Sci. Eng. A* **538**, 315 (2012).
36. J. P. Hirth and J. Lothe, *Theory of Dislocations, 2nd ed.,* John Wiley & Sons, USA (1982).
37. K. P. D. Lagerlof, *Acta Mater.* **41**, 2143 (1993).
38. M. Blicharski, *Metal Sci.* **18**, 92 (1984).
39. T. Magnin and F. Moret, *Scripta Mater.* **16**, 1225 (1982).
40. V. Vitek, R. Perrin, and D. Bowen, *Philos. Mag.* **21**, 1049 (1970).
41. V. Vitek, *Scripta Mater.* **4**, 725 (1970).
42. A. Ojha, H. Sehitoglu, L. Patriarca, and H. Maier, *Philos. Mag.* **94**, 1816 (2014).
43. C. Crussard and B. Jaoul, *Rev. Metall.* **47**, 589 (1950).
44. J.-E. Jin and Y.-K. Lee, *Mat. Sci. Eng. A* **527**, 157 (2009).
45. M. Eskandari, A. Zarei-Hanzaki, and A. Marandi, *Mater. Design* **39**, 279 (2012).
46. I. Gutierrez-Urrutia and D. Raabe, *Acta Mater.* **60**, 5791 (2012).